Polyoxometalates for continuous power generation by atmospheric humidity

Tuo Ji[1], Weilin Chen[1] (✉), Zhenhui Kang[2,3], and Liming Zhang[4]

[1] *Key Laboratory of Polyoxometalate and Reticular Material Chemistry of Ministry of Education, Northeast Normal University, Changchun 130024, China*

[2] *Institute of Functional Nano & Soft Materials (FUNSOM), Jiangsu Key Laboratory for Carbon-Based Functional Materials & Devices Department, Soochow University, Suzhou 215123, China*

[3] *Macao Institute of Materials Science and Engineering, Macau University of Science and Technology, Taipa, Macau 999078, China*

[4] *Institute of Functional State Key Laboratory of Luminescence and Applications, Changchun Institute of Optics, Fine Mechanics and Physics, Chinese Academy of Sciences, Changchun 130033, China*

ABSTRACT

Atmospheric humidity is a sustainable low-value energy widely existing in natural environment, which is a promising candidate to solve the noncontinuous and low efficiency of low-value energy power generation. Here the mono-substituted Dawson-type polyoxometalates are constructed to be highly dispersed organic ammonium-polyoxoanion clusters and are assembled into thin films power generators with micropores, working in atmospheric humidity. The optimal polyoxometalates generator with the thickness of 7.2 μm and the area of 0.36 cm² produces a voltage of 0.68 V and a current density of 19.5 μA·cm⁻² under simulated natural environment, and works continuously and stably under almost all-natural environments (humidity 10%–90%). The highly dispersed polyoxometalate nanoclusters can form microporous in polyoxometalate films to effectively absorb atmospheric humidity and spontaneously form distribution gradient of water, which is the structural basis of power generation. The continuous power generation may be maintained by the effective adsorption and utilization of H_2O, the huge electrostatic field of organic ammonium-polyoxoanion clusters, and the reasonably designed polyoxometalates containing inorganic small ions with high mobility. It is the first humidity generator designed with polyoxometalates, which may provide a new research direction for polyoxometalates in sustainable utilization of low-value energy.

KEYWORDS

atmospheric humidity, continuous power generations, nanomaterials, polyoxoanions, polyoxometalates

1　Introduction

Using the low-value energy widely distributed in natural environments to generate electricity is of great significance to the efficient utilization and sustainable development of energy [1–3]. A variety of devices have realized the collection and utilization of low-value energy, including the thermoelectric generators working at ambient temperature [4, 5], the nanogenerators using environmental micro mechanical energy [6–9], the triboelectric nanogenerators using breeze [10–12], and the solar cells working under low illumination [13, 14]. While, these devices are mainly limited by the instability and intermittency of low-value energy. It is urgent to develop a continuous low-value energy in natural environment. The atmospheric humidity is basically maintained at a high level and widely exists [15, 16], which is a continuous and stable low-value energy source with great potential applications. In recent years, great progress has been made in the utilization of atmospheric humidity energy, and its various devices have been widely developed and utilized [17–19].

The humidity was used to generate electricity by simulating the process of using water, including two main research approaches [20, 21]. Firstly, generators are designed according to the electrokinetic effects, that is, water molecules flow through the nanochannel to generate flow potential for power generation [22, 23]. Secondly, generators are designed using the principle of ion concentration cell [24, 25]. The H_2O absorbed from atmospheric humidity is used as the medium of ion movement for power generation [26, 27]. The former has higher power generation performance, especially in high humidity or assisted by other energies [28]. The latter is more adaptable to atmospheric humidity. The feasibility and application potential of humidity power generation in natural environment have been proved by both devices [29–31]. Qu et al. reported series of devices that effectively generated electricity in a wide humidity range, and further achieved a high output voltage through the absorption-ionization process of the porous ionization module [27, 32]. Yao et al. skillfully selected protein extracted from microorganisms and designed a homogeneous film generator, which generated electricity and could be repeatedly self-recharged (the ratio for charging–discharging time is about 1:4) by using the natural environment humidity [33]. This self-charging generator significantly promotes the research of natural humidity power generation.

Polyoxometalates (POMs) are a kind of nano-sized materials with special morphology and functional properties [34–42], which exhibit important application prospects in controllable synthesis, assembly, and performance research [43–50]. POM nanomaterials are expected to be the materials with the potential to effectively utilize atmospheric humidity. The reasons are as follows: (i) POM nanomaterials can self-assemble to form microporous structures [51–53], which is conducive to collecting atmospheric humidity and achieving the effective collection and utilization by adjusting the size of the POM nanomaterials [46, 54]. (ii) The POM can be ionized into polyoxoanions and cations with different migration capabilities by H_2O [55, 56]. Controlling the movement of cations and the charge density of polyoxoanions is expected to produce electrical signals [57]. (iii) POM nanomaterials are environment-friendly and have great hydrophilicity with great stability in light, heat, and chemical environment [58], which makes them have the potential to collect atmospheric humidity and work stably in the environment [59, 60]. (iv) The cations and anions, sizes, and morphologies of POM nanomaterials are adjustable [61, 62], which provides a guarantee to explore the power generation mechanism of devices to promote the in-depth research, development, and utilization of atmospheric humidity [63, 64].

Here, the mono-substituted Dawson-type POM $K_8[\alpha_2\text{-}P_2W_{17}O_{61}Cu]\cdot16H_2O$ ($P_2W_{17}Cu$) designed as highly dispersed nanowire structures was prepared into films by the simple drop-coating method and then assembled into the generators, which can genetate electricity under atmospheric humidity (Fig. 1). The water vapor adsorption experiment proves that the highly dispersed $P_2W_{17}Cu$ POM nanoclusters are stacked to form micropores, which can spontaneously collect atmospheric humidity and form the gradient distribution of H_2O in the films. The gradient distribution of H_2O induces the concentration gradient of ionized POM, which drives the directional movement of K^+ cations to generate potentials. The widely existing atmospheric humidity, dynamic adsorption–desorption process between atmosphere and $P_2W_{17}Cu$ nanowires, and the strong electrostatic field between organic ammonium cations and polyoxoanions provide the continuous energy input for generators, which realize the effective utilization of atmospheric humidity and self-charging generator without charging time in natural environment. The optimal $P_2W_{17}Cu$ nanowire generator with the thickness of 7.2 μm can produce a voltage of 0.68 V and a current density of 19.5 μA·cm^{-2} under simulated natural environment (at the atmospheric humidity of 50% and the temperature of 25 °C), and can work continuously and stably under the wide atmospheric humidity from 10% to 90%.

2 Experimental

2.1 Materials

All the raw materials used in the synthesis process were purchased from the dealers and were used directly without further purification.

2.2 Synthesis of POMs

The POMs were combined according to the method previously reported after slight modification [65]. The $Na_2WO_4\cdot2H_2O$ (0.3 mol) was dissolved in boiling water (350 mL), then the H_3PO_4 (150 mL) was dropwise added in water and the obtained solution was refluxed for 8 h. Finally, the KCl (1.4 mol) was added in solution. The pure yellow crystals $K_6[\alpha\text{-}P_2W_{18}O_{62}]\cdot14H_2O$ (P_2W_{18}) were obtained at 5 °C by recrystallizing the obtained precipitation. The P_2W_{18} (0.03 mol) was dissolved in water (300 mL, 50 °C), and the aqueous solution of $KHCO_3$ (500 mL, 1 mol·L^{-1}) was added in water under vigorous stirring. The solution was fully reacted and then the precipitate was recrystallized. The pure white product $K_{10}[\alpha_2\text{-}P_2W_{17}O_{61}]\cdot20H_2O$ (P_2W_{17}) was obtained at 5 °C. The P_2W_{17} (5 mmol) was dissolved in boiling water (100 mL), and then the aqueous solution of $CuSO_4\cdot5H_2O$ (6 mmol) ($Co(NO_3)_2\cdot6H_2O$, $Fe(NO_3)_3\cdot9H_2O$, $Ni(NO_3)_2\cdot6H_2O$, or $MnCl_2\cdot4H_2O$) was added in the above solution. After fully reacting and cooling to 5 °C, the crude product was collected. The KCl (0.2 mol) was added in the solution for $Co(NO_3)_2\cdot6H_2O$, $Fe(NO_3)_3\cdot9H_2O$, and $MnCl_2\cdot4H_2O$. The pure product $P_2W_{17}Cu$, $K_8[\alpha_2\text{-}P_2W_{17}O_{61}Co]\cdot17H_2O$ ($P_2W_{17}Co$), $K_8[\alpha_2\text{-}P_2W_{17}O_{61}Ni]\cdot17H_2O$ ($P_2W_{17}Ni$), $K_7[\alpha_2\text{-}P_2W_{17}O_{61}Fe]\cdot8H_2O$ ($P_2W_{17}Fe$), or $K_7[\alpha_2\text{-}P_2W_{17}O_{61}Mn]\cdot12H_2O$ ($P_2W_{17}Mn$) was obtained by recrystallizing the crude product.

2.3 Synthesis of POM nanowires

The highly dispersed POM nanoclusters were combined according to the method previously reported after slight modification [66]. The $P_2W_{17}M$ (1 g, M = Cu, Co, Ni, Fe, or Mn) and the KAc (0.15 g) were dissolved in water (60 mL), and the pH of the solution was adjusted to about 4.5. Tetrabutylammonium bromide (TBAB) (0.25 g) and cetyltrimethylammonium bromide (CTAB) (0.25 g) were dissolved in $CHCl_3$ (40 mL). The two solutions were mixed and the $P_2W_{17}M$ nanowires were collected at the interface. After being washed with water and evaporating at room temperature, the POM nanowire materials were obtained.

2.4 Preparation of POM nanowire generators

The POM nanowire materials (3 mg) were dissolved in $CHCl_3$ (1 mL) under stirring. And the solution was homogenized by brief ultrasound. The fluorine-doped tin oxide (FTO) glass was immersed in ethanol after being ultrasonically washed with detergent, isopropanol, and ethanol. The ethanol on the glass surface was blown dry with inert gas before use. The polyethylene terephthalate (PET)-mold was pasted onto the surface of FTO and then the FTO was placed on a stable horizontal table. Then the solution was dropped into the mold and the solvent was evaporated at room temperature to obtain POM nanowire films. The concentration of the solution remained unchanged, and 40 μL of solution was made into a film with a thickness of 1 μM and an
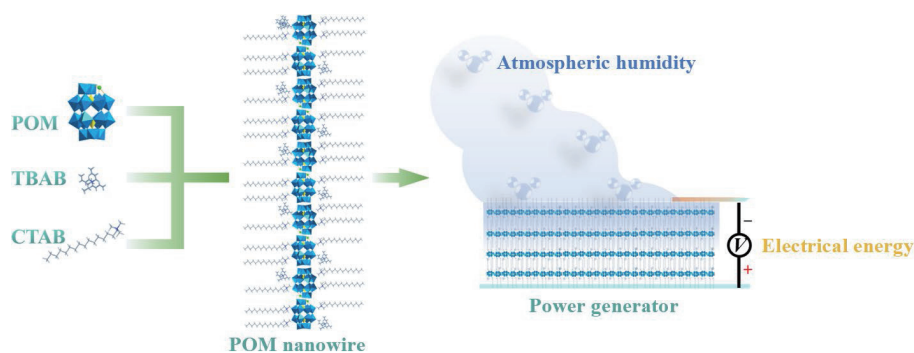

Figure 1 The schematic diagram of the formation to $P_2W_{17}Cu$ nanowires and the humidity power generators.

area of 1 cm². The cutted (3 mm × 10 mm) sticky Cu-electrode was placed on the surface of the POM nanowire film and fixed, and the area contacted with the film was 9 mm².

2.5 Characterizations

The Fourier transform infrared (FTIR) spectra were tested on AXS TENSOR-27 FTIR to characterize the basic structures of POMs and POM nanowires. The thermogravimetric analysis (TGA) was performed on PerkinElmer TGA7 instrument from 20 to 800 °C at the rate of 10 °C·min⁻¹. The range (2θ) of the small-angle X-ray scattering (SAXS) was from 1° to 10°, and uniformly pressed sheets of POM nanowires were used as the test samples. The powder X-ray diffraction (XRD) data were collected from a Bruker AXS D8 Advanced Bruker with Cu Kα radiation in the 2θ range from 5° to 80°. The X-ray photoelectron spectroscopy (XPS) was performed on a Thermo SCIENTIFIC ESCALAB 250Xi spectrometer by utilizing Al Kα radiation as the X-ray source. The transmission electron microscopy (TEM) was performed on a JEM-2100F. The field emission scanning electron microscopy (SEM) was characterized by HITACHI SU8010.

2.6 Test of electrical performance

All the tests were done on the Electrochemical workstation CHI760e (Shanghai-Chenhua), the Digital Source-meter Keithley 6514, and the Electrochemical workstation ParStat4000 (Ametak-Princeton).

2.7 Simulation and control of atmospheric humidity

The wet air with relative humidity of 100% and the dry air with relative humidity of 0% were evenly mixed in a certain proportion, and then the mixed gas was introduced into the operation box. The relative humidity of the mixture was controlled by changing the ratio of the two gases. Thus, the atmospheric humidity under different experimental conditions was simulated according to the experimental intention. The values of atmospheric humidity were monitored by a hygrometer.

3 Results and discussion

3.1 The properties of P₂W₁₇Cu and P₂W₁₇Cu nanowires

The P₂W₁₇Cu was synthesized according to Ref. [67], which was proved by powder XRD and FTIR (Fig. S1 in the Electronic Supplementary Material (ESM)). The highly dispersed P₂W₁₇Cu nanowires were prepared with CTAB and TBAB in the mixed liquid of water and chloroform by the two-phase interface synthesis approach (Fig. 2(a)) (more informations about synthesis can be found in the Experimental section).

The ultra-fine flexible structure of POM nanowires is beneficial for the high dispersion of POM and conducive to the formation of micropores, which is instrumental in the absorption and the utilization of atmospheric humidity. Other nanowires with different POMs were synthesized by the same mathod (Figs. S2 and S3 in the ESM) [67]. The TEM image indicates that the diameter of P₂W₁₇Cu nanowires is only about 1 nm and the length is at the micron level (Fig. 2(b)). The high-resolution TEM image (the inset of Fig. 2(b)) directly proves that the polyoxoanions in P₂W₁₇Cu nanowires are dispersedly arranged, which is conducive to the effective contact between P₂W₁₇Cu POM nanoclusters and H₂O molecules. The energy dispersive X-ray spectroscopy (EDS) mapping measurement verifies the existence of K, N, Cu, P, and W, which uniformly distributed in the P₂W₁₇Cu nanowires (Fig. S4 in the ESM).

The FTIR spectra (Fig. 2(c)) show that the polyoxoanions structure (600 to 950 cm⁻¹) and the organic ammonium cations

(3800 to 3900 cm⁻¹) exist in the P₂W₁₇Cu nanowires [68]. The SAXS curve of P₂W₁₇Cu nanowires shows two obvious peaks at 2θ = 2.92° and 2θ = 7.08° (the inset of Fig. 2(d)), which is related to the dispersibility of polyoxoanions [69]. The XRD pattern (2θ = 5°–50°) of P₂W₁₇Cu nanowires shows almost a horizontal line, and the XRD peaks shown by the original P₂W₁₇Cu, CTAB, and TBAB are disappeared after forming nanowires (Fig. 2(d)), which is because P₂W₁₇Cu nanowires are not in crystal state. The XRD and SAXS results of the P₂W₁₇Cu nanowires indicate that the polyoxoanions are highly dispersed by forming the nanowire structure [70]. The XPS test proves the existence of stable polyoxoanions, organic ammonium cations, and K⁺ cations (Fig. S5 in the ESM) [71–74]. According to TGA curves (Fig. 2(e)), the molecular formula of the nanowire structure is {K₄(TBA)(CTA)₃[P₂W₁₇O₆₁Cu]·3H₂O}$_n$ (the detailed data are listed in Table S1 in the ESM). The cyclic voltammetric (CV) curve of P₂W₁₇Cu nanowires (Fig. 2(f)) shows a pair of redox peaks, which is attributed to the W(VI)/W(V) transformation in the polyoxoanions [75, 76] (detailed data are displayed in Fig. S6 in the ESM). The above characterizations prove that the POM nanowires are inorganic material based on POMs, but show the properties of polymer-like materials by forming 1 nm nanowires, such as non-crystallinity, flexibility, transparency, and simple and good film-forming properties, which are conducive to their development and utilization in humidity generators.

3.2 The preparation, structure, and performances of P₂W₁₇Cu nanowire generators

The P₂W₁₇Cu nanowires were made into thin films by drop-coating and assembled into electric generators (Fig. 3(a)). FTO glass was used as the bottom electrode after being cleaned, then the PET-mold was placed and fixed on FTO glass (Fig. 3(a)(i)). The chloroform solution of P₂W₁₇Cu nanowires was added in the mold and evaporated slowly at room temperature (Figs. 3(a)(ii) and 3(a)(iii)). Then the mold was removed, and a Cu-electrode was added to assemble the generator (Figs. 3(a)(iv) and 3(a)(v)) (the details of generator preparation are shown in the Experimental section).

The field emission SEM images show that the films are flat and uniform (Fig. 3(b) and Fig. S7 in the ESM), and the elements of P₂W₁₇Cu nanowires are evenly distributed on the film (Fig. S7 in the ESM). The polyoxoanions in the P₂W₁₇Cu nanowires are arranged in beaded shape, and the diameter of the nanowires is only about 1 nm (Fig. 3(b)). Therefore, the nanowires and the micropores formed by the stacking of materials can not be observed in the SEM images, but the flat membrane in the state of polymer-like membrane can be observed. The atomic force microscopy (AFM) test results are shown in Fig. S8 in the ESM that the P₂W₁₇Cu nanowires were evenly distributed on the FTO substrate, showing a dispersed morphology similar to that in TEM results. The P₂W₁₇Cu nanowire generator includes FTO glass conductive layer as the negative electrode, P₂W₁₇Cu nanowire film as the working layer, and Cu-electrode as the positive electrode (Figs. 3(c) and 3(d)). The layered structure of obtained P₂W₁₇Cu nanowire generator can be observed from the cross-sectional view of SEM image (Fig. 3(e)). The water contact angle test results show that the water contact angle on the surface of the P₂W₁₇Cu nanowire films is about 45° at 30 s (Fig. S9 in the ESM), indicating that the P₂W₁₇Cu nanowire films have great hydrophilicity and hygroscopic effect. Figure 3(c) shows a photo of the P₂W₁₇Cu nanowire generator with an area of 3.24 cm² and a thickness of 7.2 μm (1.8 cm × 1.8 cm × 7.2 μm, all the generators are described by the size of the POM nanowire film). The overall photo is an FTO glass with a size of 2.25 cm × 2.5 cm and the part surrounded by gray dotted line is the P₂W₁₇Cu nanowire film with a size of
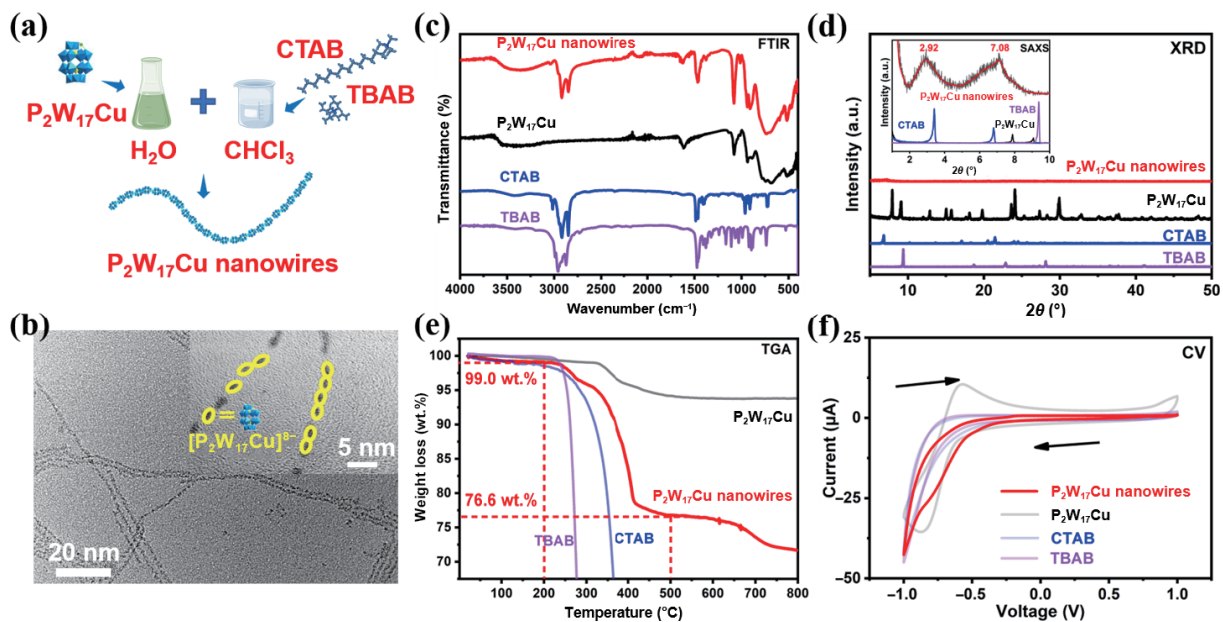
Figure 2 The synthesis, structure, and characterizations of $P_2W_{17}Cu$ and $P_2W_{17}Cu$ nanowires. (a) The schematic diagram of synthesis process for $P_2W_{17}Cu$ nanowires. The cetyltrimethylammonium canions and tetrabutylammonium canions (CTA^+ and TBA^+) are omitted in the structure diagram of $P_2W_{17}Cu$ nanowires. (b) The TEM image and high-resolution TEM image (inset) of $P_2W_{17}Cu$ nanowires. The dark parts circled by the yellow color ellipses are the polyoxoanions $[P_2W_{17}Cu]^{8-}$ of $P_2W_{17}Cu$ nanowires. (c) The FTIR spectra, (d) XRD patterns and SAXS patterns (inset), (e) TGA curves, and (f) CV curves in the range of −1 to 1 V of $P_2W_{17}Cu$ (black), CTAB (blue), TBAB (purple), and $P_2W_{17}Cu$ nanowires (red).

1.8 cm × 1.8 cm. It can be observed that the pattern at the bottom of FTO glass can be well observed through the generator, indicating that the generator has good light transmission performance. The ultraviolet–visible (UV–vis) test results (Fig. S10 in the ESM) indicate that the $P_2W_{17}Cu$ nanowire films possess high transparency, proving that the internal structure of which is uniform. The high transparency of the $P_2W_{17}Cu$ nanowire generator is conducive to its wider application in all aspects of production and life.

The performance of the $P_2W_{17}Cu$ nanowire generator was evaluated by monitoring the open circuit voltage (V_{oc}) and the short circuit current (J_{sc}) of different generators. The chronoamperometric and chronopotentiometric tests show that the $P_2W_{17}Cu$ nanowire generators have continuous power generation performance, and one $P_2W_{17}Cu$ nanowire generator with an area of 0.36 cm^2 and a thickness of 7.2 μm can produce a voltage of about 0.7 V and current of 7 μA (current density of 19 μA·cm^{-2}) at the atmospheric humidity of 50% and the temperature of 25 °C (Fig. 3(f)). The current and voltage of the above one $P_2W_{17}Cu$ nanowire generator were continuously monitored for a long time in a stable environment. The results show that the output current and voltage of the generator are stable for more than 6 days without stopping (Fig. S11 in the ESM), proving that the POM nanowire generator does not require complex processing, but can spontaneously restore its power generation capacity, that is, the self-charging generator, and can be used to integrate with electrical equipment in future practical applications to realize the self-power supply. The cycle performance testing of $P_2W_{17}Cu$ nanowire generator shows that the power generation performance remains basically unchanged after 50 cycles of drying and power generation treatment (Fig. S12 in the ESM), proving that the generator has good stability and cycling performance. The test that monitor the J_{sc} and V_{oc} of $P_2W_{17}Cu$ nanowire generators under the atmospheric humidity from 10% to 50% (Fig. 3(g)) shows that the J_{sc} and V_{oc} increased significantly with the increase of humidity (Figs. 3(g) and 3(h)), and the continuous increase of atmospheric humidity obtains a slight increase of the J_{sc} and V_{oc} (Fig. 3(h)). It is proved that the performance of the $P_2W_{17}Cu$ nanowire generator depends on the

value of atmospheric humidity under the condition of constant temperature and reaches the nearly saturated state after the atmospheric humidity is more than 50%.

Figure 3(i) shows that the V_{oc} increases from 0.46 to 0.74 V with the thickness increasing from 2.4 to 9.6 μm, which may be attributed to that the increasing thickness can promote the further uneven distribution of more charges in the space of the $P_2W_{17}Cu$ nanowire film. For the current, the firstly increased and then decreased trend may be caused by the fact that the increase of the thickness raises the charge density of $P_2W_{17}Cu$ nanowire generators, but blocks the transport of charges. The negative impact of charge transmission damage will cause the current to greatly reduce as the charge value approaches the maximum. Therefore, the feasible scheme to improve the output performance of the $P_2W_{17}Cu$ nanowire generator is to improve the transmission performance of the material. The J_{sc} and V_{oc} of $P_2W_{17}Cu$ nanowire generators reduce with the decline of temperature, but the generators can work normally even at a low temperature of −10 °C (Fig. 3(j)), proving that the H_2O used by the $P_2W_{17}Cu$ nanowire generator in the power generation process is gaseous H_2O rather than liquid H_2O. Liquid H_2O will freeze at the temperature below zero, while gaseous H_2O molecules can exist, which makes our generator have a wider range of applications and can adapt to the worse temperature environment. The reduction of temperature will lead to the reduced content of H_2O in the atmosphere at the same relative humidity value. The calculation of H_2O content at different temperatures (Table S2 in the ESM) shows that low temperature has little impact on the performance of the device, but high temperature (higher than 50 °C) will reduce the operating performance of the device (compared with the environment at 25 °C with the same H_2O content), which can be attributed to that the temperature affects the motion of charged particles in the $P_2W_{17}Cu$ nanowire film. Based on the above experimental results, it is predicted that the $P_2W_{17}Cu$ nanowire generator has the highest operating ability in the environment at 20 °C (about 0.1 higher than that of 25 °C) and high power generation performance at 10 to 40 °C in practical application.
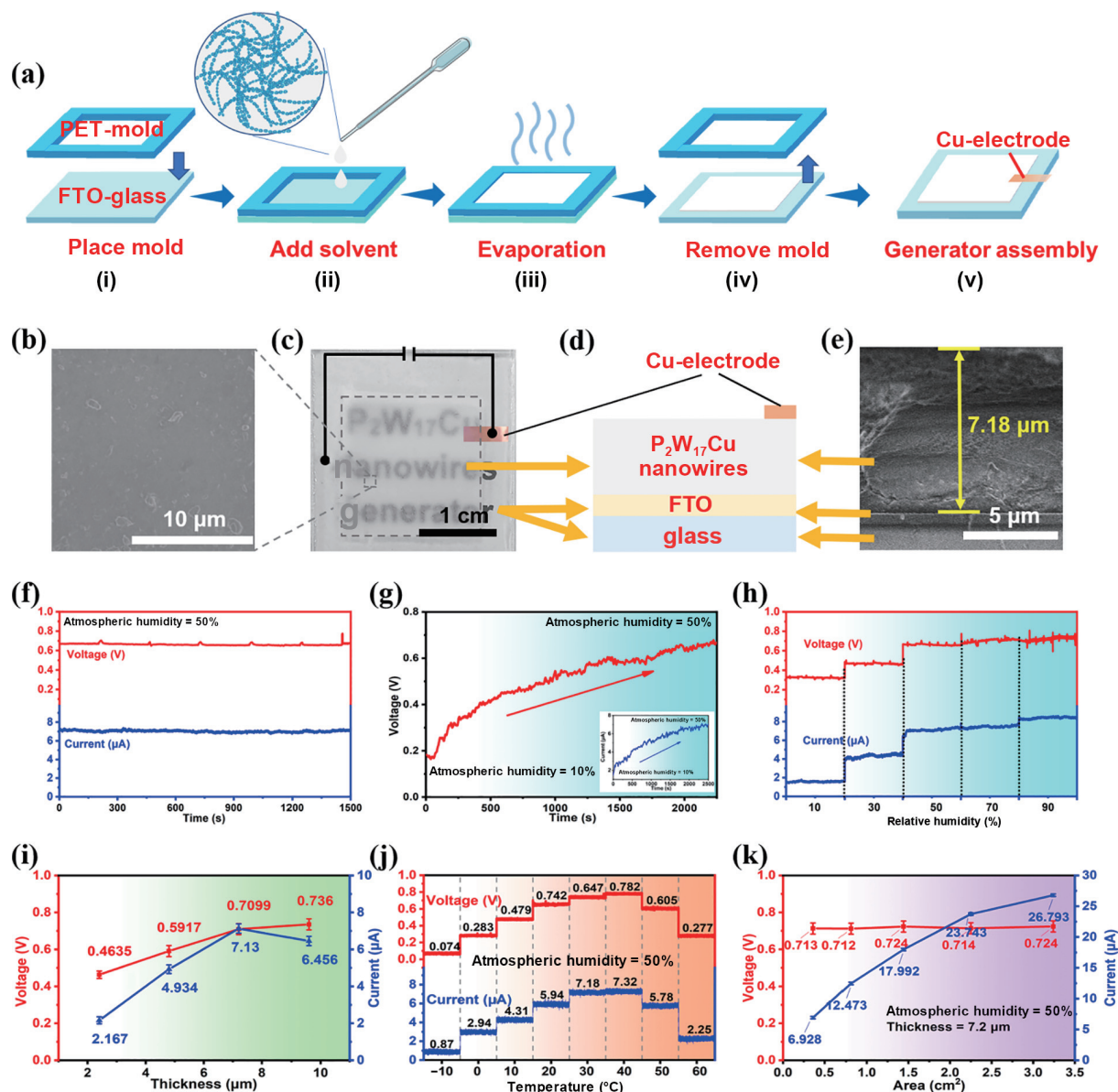
Figure 3 The preparation, structure, and performances of $P_2W_{17}Cu$ nanowire generators. (a) The preparation of $P_2W_{17}Cu$ nanowire films: (i) The PET-mold is placed on the clean FTO-glass. (ii) The chloroform solution of $P_2W_{17}Cu$ nanowires is added in the PET-mold. (iii) The evaporation process of chloroform solvent is carried out at room temperature. (iv) The PET-mold is removed and the $P_2W_{17}Cu$ nanowire film is coated on the surface of FTO. (v) The generator is assembled by adding Cu-electrode. (b) The superficial SEM image of a $P_2W_{17}Cu$ nanowire generator. (c) The photo of a $P_2W_{17}Cu$ nanowire generator. (d) The structure diagram of $P_2W_{17}Cu$ nanowire generators. (e) The cross-sectional SEM image of a $P_2W_{17}Cu$ nanowire generator. (f) The V_{oc} and J_{sc} under stable atmospheric humidity of 50%. (g) The V_{oc} and J_{sc} (inset) monitored as atmospheric humidity changes from 10% to 50%. The power generation performance of $P_2W_{17}Cu$ nanowire generators under different (h) atmospheric humidities, (i) thicknesses, (j) temperatures, and (k) areas.

Figure 3(k) shows that the V_{oc} changes little with the increase of the generator area and the J_{sc} increases significantly, but the current density reduces significantly (Fig. S13 in the ESM), proving that the small area of generators is conducive to the transmission of charges (detailed data are listed in Tables S3–S6 in the ESM). The generation of voltage is related to the longitudinal process of the $P_2W_{17}Cu$ nanowire film, and the increased area of $P_2W_{17}Cu$ nanowire film affects the collection of charge to a certain extent, resulting in the decrease of current density. The $P_2W_{17}Cu$ nanowires are prepared into ordered structure and assembled into the generator by improved preparation process of the generator (Figs. S14 and S15 in the ESM). The results indicate that an ordered structure is beneficial for optimizing the internal resistance of the generator (Fig. S16 in the ESM) [77–79].

Therefore, in addition to developing new materials, the improvement of structure and morphology of POM nanowires and the design and research of porous electrodes are of great significance to promote the development of atmospheric humidity generators. The power generation performance testing shows that the generator can continue to operate effectively in the natural environment with the humidity of about 10% to 50% and the temperature of 5 to 22 °C, proving that the generator can indeed work stably in indoor and outdoor environments (Fig. S17 in the ESM).

The parallel experiments show that the generator with the optimal thickness and area of 7.2 μm and 0.36 cm^2 has high generation capability at room temperature under humidity higher than 50%. The $P_2W_{17}Cu$ nanowire generators can work stably in almost all indoor and outdoor natural environments, and have broad application prospects with the simple preparation method. The response performance test of the generator to sudden applied humidity shows that the response time was about 1.5 s (Fig. S18 in the ESM), proving that the device can be used for rapid humidity detection and alarm systems, which has feasible application

prospects in human health monitoring and environmental humidity detection and control.

3.3 The output performance of different $P_2W_{17}Cu$ nanowire generators

A series of tests were carried out to explore the generation reason of the electric signals. The test reversing the electrode shows that the voltage changes from positive to negative, but the value is basically unchanged (Fig. 4(a)), proving that the cathode of the $P_2W_{17}Cu$ nanowire generator is the FTO glass electrode that insulates the atmospheric humidity from the $P_2W_{17}Cu$ nanowire film and the anode is the Cu-electrode. The power generation performance of the $P_2W_{17}Cu$ nanowire generator using inert Pt/Pt electrode to replace the FTO glass and Cu-electrode was tested, and the V_{oc} and J_{sc} values similar to those of the original device were obtained (Fig. S19 in the ESM). The side effects of the device are eliminated through the above inert electrode experiment, proving that the electric signals are generated not from the chemical reactions between the electrodes and the $P_2W_{17}Cu$ nanowire films, but from the $P_2W_{17}Cu$ nanowire films themselves. POM materials usually have good photosensitive properties. The optical power value in the testing environment and the ratio of photocurrent to dark-current under AM 1.5 G were tested to eliminate the impact of light on performance evaluation (Fig. S20 in the ESM). POM nanowires do indeed have good photo-responsive properties, and high-power sunlight exposure was avoided during testing (the average optical power value is only 0.1 W·cm^{-2} under the test conditions) to truly and reliably obtain the ability of POM nanowire generators to utilize humidity and generate electricity. The output performance of the $P_2W_{17}Cu$ nanowire generator was tested by connecting resistors with different resistance values in parallel or in series. It is found that the output voltage of the generators gradually increases with the increase of the resistance values and the current gradually decreases (Fig. 4(b)). The maximum output power density is about 0.1 mW·cm^{-3} when the resistance value is about 50 kΩ (Fig. 4(c)).

Figures 4(d)–4(i) show the response of the J_{sc} and V_{oc} by different generators to atmospheric humidity (between 10% and 50%) with the 100 s time intervals. The $P_2W_{17}Cu$ nanowire generators have a high dependence on atmospheric humidity, proving that the existence of humidity is the primary condition for the power generation. And the materials with different morphologies and compositions were synthesized to explore the mechanism of generators. Firstly, the generator made of $P_2W_{17}Cu$ non nanowire has poor power generation capacity, and 50 nm $P_2W_{17}Cu$ nanowires do not generate electricity, indicating that the dimension of nanowires has great impact on the power generation capacity (Figs. 4(d) and 4(g)). The main impact of morphology on devices lies in the size of micropores, so designing materials rich in micropores with appropriate sizes is an important direction for material development. Secondly, no electrical signal is produced when there is only organic ammonium cations or K$^+$ cations existed in the nanowires, showing that the simultaneous existence of the two kinds of cations is the basic condition to generate electricity (Figs. 4(e) and 4(h)). Regulating the composition of cations is expected to further improve the generation performance. Thirdly, the generators still show high power generation performance when K$^+$ cations are replaced by Na$^+$ cations (Na-$P_2W_{17}Cu$ nanowires), while Cs-$P_2W_{17}Cu$ nanowires are not, proving that the capacity of the generators is related to the migration capacity of cations in the nanowires (Figs. 4(f) and 4(i)). Therefore, improving the ion migration kinetics within the device through material design is an important direction for improving

output power. Finally, the stable power generation performance of different generators with different structures and components of POM nanowires with temperature at 25 °C and atmospheric humidity at 50% is shown in Fig. S21 in the ESM. The power generation performance is basically unchanged when the polyoxyanions are replaced by [$P_2W_{17}Co$]$^{8-}$ ($P_2W_{17}Co$ nanowires, Fig. S21(a) in the ESM), proving that the kinds of metal elements in the polyoxyanions have little influence on the power generation performance (the TEM images and continuous power generation performance of the materials are shown in Figs. S22–S24 in the ESM). Figure S25 in the ESM shows the specific J_{sc} and V_{oc} values of the above generators. In summary, for POM humidity generators, orderly and rich microporous structures with appropriate sizes, effective and reasonable design of cations, and efficient and stable ion migration performance are feasible paths for material development.

3.4 The mechanism of the $P_2W_{17}Cu$ nanowire generators

As shown above, the highly dispersive $P_2W_{17}Cu$ POM with the organic ammonium-polyoxoanion cluster structure is the important basic condition for building generators, which can be ionized to produce polyoxoanions and K$^+$ cations with different properties. Also, all the results suggest that the dynamic process of adsorption–desorption maintained by atmospheric humidity supports the performance of continuous power generation and self-charging of the generator.

The $P_2W_{17}Cu$ nanowire generator involves two important processes of two charged particles during its operation: the movement of electrified H$_2$O molecules and the diffusion of K$^+$ cations (Fig. S26 in the ESM). The strong electrostatic field can drive the electrification of molecules, promoting electron transfer [80, 81]. Polyoxyanions have high charge capacity and stable structure, forming a large electrostatic field between polyoxyanions and organic ammonium cations. The process of H$_2$O molecules electrification is completed by the strong electrostatic field in the $P_2W_{17}Cu$ POM nanoclusters [81, 82], which completes the charge transfer and ensures that the atmospheric humidity continuously provides energy input for the generator (Fig. S26(a) in the ESM). The directional movement of K$^+$ cations causes the $P_2W_{17}Cu$ nanowir film to generate an internal electric field, which generates voltage and drives the movement of electrified H$_2$O molecules to generate current (Fig. S26(b) in the ESM). And the existence of distribution gradient induced by atmospheric humidity supports the formation of electric field and drives the continuous power generation.

The formation of electric field in the $P_2W_{17}Cu$ nanowir film is based on the gradient distribution of H$_2$O and the free diffusion process of K$^+$ cations, which can be expressed according to Fick's second law. And the electrical output will be balanced with the moisture absorption of the $P_2W_{17}Cu$ nanowire films under the quasi-steady state (Fig. S27 in the ESM). The voltage generated by the ion gradient (U) and the current generated by the movement of charged particles (I) can be expressed by Eqs. (1) and (2) as follows (the detailed derivation is shown in the ESM) [83, 84]

$$I = \frac{N_A}{n} \times \frac{SC_0}{2}\sqrt{\frac{D}{t}} = 4.82 \times 10^4 \times SC_0\sqrt{\frac{D}{t}} \quad (1)$$

$$U = 4.82 \times 10^4 \times SC_0\sqrt{\frac{D}{t}}R \quad (2)$$

where S is the effective area perpendicular to the diffusion direction (the area of $P_2W_{17}Cu$ nanowire films), D is the diffusion coefficient, C_0 is the initial concentration of ions, N_A is Avogadro
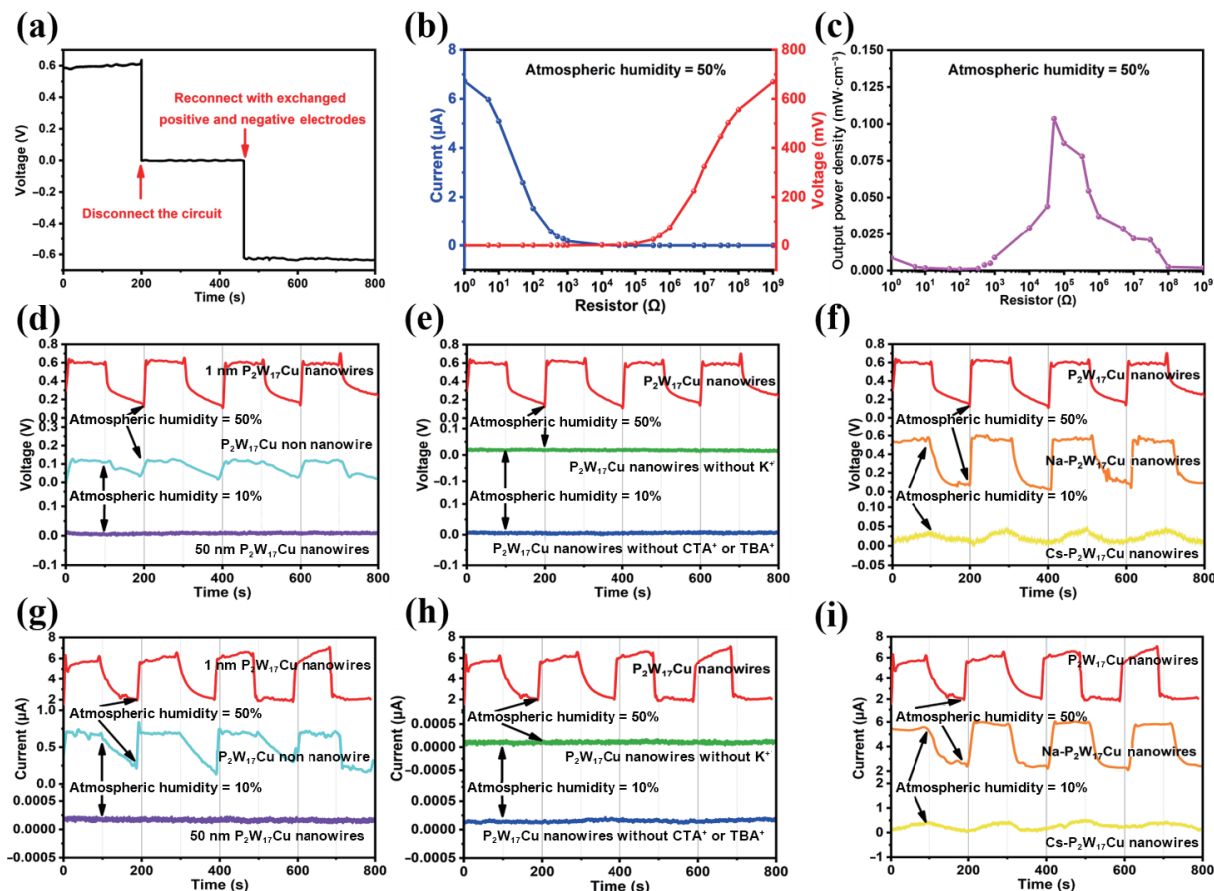
Figure 4 The output performance of different $P_2W_{17}Cu$ nanowire generators. (a) The V_{oc} monitored during electrode reverse connection. (b) The output voltage and current of $P_2W_{17}Cu$ nanowire generator load with different resistance values with the atmospheric humidity at 50% and temperature at 25 °C . (c) The power density of generator under different resistance loads. (d)–(f) The current and (g)–(i) voltage of generators made of different materials, for which the voltage and current of the generator with different morphologies are shown in (d) and (g), different compositions in (e) and (h), and different cations in (f) and (i). The 1 nm $P_2W_{17}Cu$ nanowire generator in red, the $P_2W_{17}Cu$ non nanowire generator in cyan, the generator of 50 nm $P_2W_{17}Cu$ nanowire in purple, the generators of nanowires without K^+ cations in green and without organic ammoniums (CTA^+ and TBA^+) in bule, the Na-$P_2W_{17}Cu$ nanowire generator in orange, and the Cs-$P_2W_{17}Cu$ nanowire generator in yellow.

constant (6.02×10^{23}), n is the number of electrons per Coulomb, t is the diffusion time, and R is the resistance (Ω) of $P_2W_{17}Cu$ nanowire films, respectively.

The mechanism of $P_2W_{17}Cu$ nanowire generators is proposed on the basis of all the above experimental results and analyses, as shown in **Fig. 5**, which consists of four parts, namely, (i) the adsorption of atmospheric humidity and formation of H_2O distribution gradient, (ii) the ionization of POMs and the concentration gradient of ions, (iii) the directional movement of K^+ cations and generation of electric field, and (iv) the dynamic adsorption–desorption process and self-charging.

Firstly, the adsorption of atmospheric humidity and formation of H_2O distribution gradient are the basic conditions for the power generations (Fig. 5(a)). Water molecule adsorption experiments of $P_2W_{17}Cu$ show that POMs have good hygroscopicity (Fig. S28 in the ESM), which is because POMs are hydrophilic materials that can absorb part of H_2O and make it exist on the surface of POM molecules. The surface exposure rate of $P_2W_{17}Cu$ molecules is higher after the formation of $P_2W_{17}Cu$ nanowires with sub-nanometer diameter, and the adsorption capacity of H_2O is also stronger. At the same time, when the film is formed, the $P_2W_{17}Cu$ nanowires will stack to form micropores. More H_2O molecules in the atmosphere are spontaneously absorbed by $P_2W_{17}Cu$ nanowire films to form the distribution gradient of H_2O due to capillary effect (Fig. S29(a) in the ESM). The content of H_2O gradually decreases from the top (the surface contacting with air) to the bottom (the inner surface contacting with FTO) of $P_2W_{17}Cu$ nanowire films. The water vapor

adsorption–desorption test (Fig. S29(b) in the ESM) shows that the 1 nm nanowire films have strong adsorption–desorption capacity, and proves that the micropores in the films certainly restrict and control the adsorption–desorption process of atmospheric humidity to form H_2O distribution gradient.

Secondly, the ionization of POMs and the concentration gradient of K^+ cations are the necessary conditions for $P_2W_{17}Cu$ nanowire films to generate electricity (Fig. 5(b)). POMs, as hydrophilic clusters, are easy to be ionized by H_2O to form the concentration gradients of ions between the top and bottom of $P_2W_{17}Cu$ nanowire films depending on the distribution gradient of H_2O. The electrical conduction tests show that the conductivity of the $P_2W_{17}Cu$ nanowire films increases with the increase of atmospheric humidity (Fig. S30 in the ESM). The conductivity of the $P_2W_{17}Cu$ nanowire films increases from 0.000235 to 0.0818 $S·m^{-1}$ with the humidity from 10% to 90% (Fig. S30(a) in the ESM), which reflects that the ionization of $P_2W_{17}Cu$ nanowires is accompanied by the adsorption of H_2O and leads to the effective movement of ions in the membrane to transfer charges.

Thirdly, the directional movement of K^+ cations and generation of electric field are the key points for $P_2W_{17}Cu$ nanowire power generations (Fig. 5(c)). As reported, the migration rate of K^+ cations is about 63 times higher than that of polyoxoanions under the same conditions. The migration rate of Na^+ cations is 101 times higher than polyoxoanions, and the migration rate of Cs^+ cations is 46 times higher than polyoxoanions (Table S7 in the ESM), since the ion migration ability is related to the mass and volume [85, 86]. Moreover, the migration of polyoxoanions in the
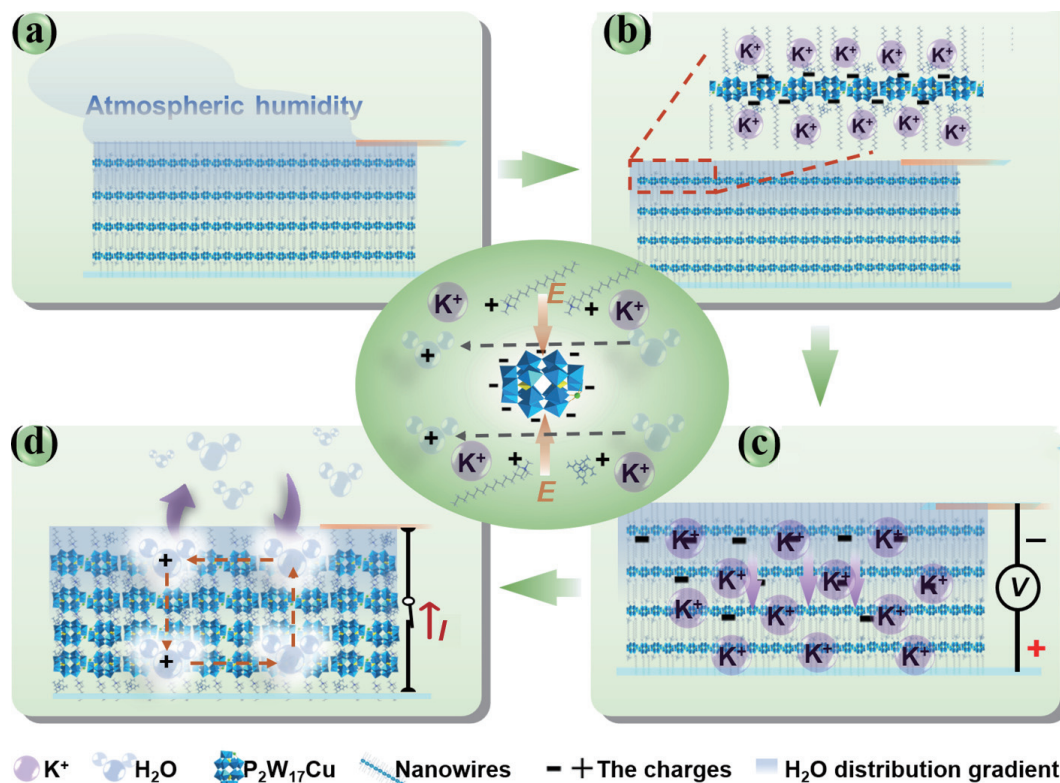
Figure 5 The mechanism of the $P_2W_{17}Cu$ nanowire generators. (a) The adsorption of atmospheric humidity and formation of H_2O distribution gradient. (b) The ionization of POMs and the concentration gradient of ions. (c) The directional movement of K^+ cations and generation of electric field. (d) The dynamic adsorption–desorption process and self-charging. The middle illustration shows the working state of the $P_2W_{17}Cu$ POM nanocluster in the $P_2W_{17}Cu$ nanowire generators. (a)–(d) Parts of the mechanism simultaneously exist in $P_2W_{17}Cu$ nanowire generators when the generators generate electricity by atmospheric humidity.

water is limited by the stronger electric field formed by the higher charge content. And this multiple will be further expanded by the limitation of the size of micropores, which leads to the negligible movement of polyoxoanions for K^+ and other small volume cations in this system. The K^+ cations spontaneously diffuse from high concentration to low concentration due to the concentration gradient, while the polyoxoanions relatively do not move. Therefore, the positive charges are accumulated at the inner surface, and negative charges are accumulated on the outer surface, thus forming the electric field (Fig. S27(a) in the ESM). The direction of the electric field is from the bottom (not in contact with atmospheric humidity) to the top (in contact with atmospheric humidity) of $P_2W_{17}Cu$ nanowire films, which can also be proved by the electrode reverse connection experiment (Fig. 4(a)). It is worth noting that Fig. S11 in the ESM shows that the generation of current and voltage is stable, not the common rapid discharge process of K^+ cations movement, proving that the main effect for the movement of K^+ cations is to form a relatively stable electric field, and the relatively stable electric output is maintained by other processes.

Finally, the dynamic adsorption–desorption process and electrification–de-electrification process are the foundations for the stable operations of $P_2W_{17}Cu$ nanowire generators (Fig. 5(d)). POMs have strong electron harvesting ability, and capture the electrons of H_2O molecules and transfer them to the external circuit with the excitation of strong electrostatic field. The electrical activity of H_2O molecules is excited by strong electrostatic field and promotes the process of electron transfer. The electrifying process of H_2O molecules is equivalent to completing the charge transfer between $P_2W_{17}Cu$ POM nanoclusters and H_2O molecules, and realizing the conversion of atmospheric humidity energy to electrical energy. The atmospheric humidity energy is continuously captured by the $P_2W_{17}Cu$ POM nanoclusters and is used for power generation by

dynamic adsorption–desorption processes. As the external circuit is connected, the electrified H_2O molecules will move to complete the charge transfer between the upper and lower surfaces of the $P_2W_{17}Cu$ nanowire film (Fig. S27(b) in the ESM), which is driven by the built-in electric field generated by the directional movement of K^+ cations. Altogether, the strong electrostatic field between organic ammonium cation and polyoxyanion is the driving force for electron transfer, and the continuous adsorption–desorption process promotes the distribution gradient of H_2O molecules and uneven distribution of charges. Both provide continuous energy input for POM nanowire power generator and induce continuous current generation and continuous electrical output.

4　Conclusions

The $P_2W_{17}Cu$ nanowire generators realize the utilization of atmospheric humidity as environmental low-value energy. The investigations show that electric generator can produce potentials by spontaneously absorbing atmospheric humidity with the micropores in POM nanowire films. In this process, the existence of micropores, organic ammoniums, polyoxoanions, and K^+ cations plays a vital role on the power generations, the size of nanowires and the migration ability of ions are the important factors of affecting the power generation performance of the generators, and the developments and optimizations of which can further improve the power generation performance of humidity electric generator. The $P_2W_{17}Cu$ nanowire generators have high stability and continuous power generation performance, which behave wide application prospects in indoor and outdoor power generations, self-power supply, and self-charging, and provide a new idea for the development of POMs.

Acknowledgements

References

[1] Hong, H. X.; Yang, X. Y.; Cui, H.; Zheng, D.; Wen, H. Y.; Huang, R. Y.; Liu, L. Q.; Duan, J. L.; Tang, Q. W. Self-powered seesaw structured spherical buoys based on a hybrid triboelectric–electromagnetic nanogenerator for sea surface wireless positioning. *Energy Environ. Sci.* **2022**, *15*, 621–632.

[2] Wang, T.; Ji, T.; Chen, W. L.; Li, X. H.; Guan, W.; Geng, Y.; Wang, X. L.; Li, Y. G.; Kang, Z. H. Polyoxometalate film simultaneously converts multiple low-value all-weather environmental energy to electricity. *Nano Energy* **2020**, *68*, 104349.

[3] Guerra, O. J.; Zhang, J. Z.; Eichman, J.; Denholm, P.; Kurtz, J.; Hodge, B. M. The value of seasonal energy storage technologies for the integration of wind and solar power. *Energy Environ. Sci.* **2020**, *13*, 1909–1922.

[4] Davids, P. S.; Kirsch, J.; Starbuck, A.; Jarecki, R.; Shank, J.; Peters, D. Electrical power generation from moderate-temperature radiative thermal sources. *Science* **2020**, *367*, 1341–1345.

[5] Zheng, Y. Y.; Han, X.; Yang, J. W.; Jing, Y. Y.; Chen, X. Y.; Li, Q. Q.; Zhang, T.; Li, G. D.; Zhu, H. T.; Zhao, H. Z. et al. Durable, stretchable, and washable inorganic-based woven thermoelectric textiles for power generation and solid-state cooling. *Energy Environ. Sci.* **2022**, *15*, 2374–2385.

[6] Gao, M. Y.; Wang, P.; Jiang, L. L.; Wang, B. W.; Yao, Y.; Liu, S.; Chu, D. W.; Cheng, W. L.; Lu, Y. R. Power generation for wearable systems. *Energy Environ. Sci.* **2021**, *14*, 2114–2157.

[7] Jing, Z. X.; Zhang, J. C.; Wang, J. L.; Zhu, M. K.; Wang, X. X.; Cheng, T. H.; Zhu, J. Y.; Wang, Z. L. 3D fully-enclosed triboelectric nanogenerator with bionic fish-like structure for harvesting hydrokinetic energy. *Nano Res.* **2022**, *15*, 5098–5104.

[8] Zhang, S.; Jing, Z. X.; Wang, X. X.; Zhu, M. K.; Yu, X.; Zhu, J. Y.; Cheng, T. H.; Zhao, H. W.; Wang, Z. L. Soft-bionic-fishtail structured triboelectric nanogenerator driven by flow-induced vibration for low-velocity water flow energy harvesting. *Nano Res.* **2023**, *16*, 466–472.

[9] Gong, S.; Yap, L. W.; Zhu, B. W.; Zhai, Q. F.; Liu, Y. Y.; Lyu, Q. X.; Wang, K. X.; Yang, M. J.; Ling, Y. Z.; Lai, D. T. H. et al. Local crack-programmed gold nanowire electronic skin tattoos for in-plane multisensor integration. *Adv. Mater.* **2019**, *31*, 1903789.

[10] Sun, W. P.; Ding, Z.; Qin, Z. Y.; Chu, F. L.; Han, Q. K. Wind energy harvesting based on fluttering double-flag type triboelectric nanogenerators. *Nano Energy* **2020**, *70*, 104526.

[11] Wang, Y.; Chen, T. Y.; Sun, S. W.; Liu, X. Y.; Hu, Z. Y.; Lian, Z. H.; Liu, L.; Shi, Q. F.; Wang, H.; Mi, J. C. et al. A humidity resistant and high performance triboelectric nanogenerator enabled by vortex-induced vibration for scavenging wind energy. *Nano Res.* **2021**, *15*, 3246–3253.

[12] Wang, Y.; Wang, J. Y.; Xiao, X.; Wang, S. Y.; Kien, P. T.; Dong, J. L.; Mi, J. C.; Pan, X. X.; Wang, H. F.; Xu, M. Y. Multi-functional wind barrier based on triboelectric nanogenerator for power generation, self-powered wind speed sensing and highly efficient windshield. *Nano Energy* **2020**, *73*, 104736.

[13] Bai, J. X.; Huang, Y. X.; Wang, H. Y.; Guang, T. L.; Liao, Q. H.; Cheng, H. H.; Deng, S. H.; Li, Q. K.; Shuai, Z. G.; Qu, L. T. Sunlight-coordinated high-performance moisture power in natural conditions. *Adv. Mater.* **2022**, *34*, 2103897.

[14] Wang, G.; Huang, R.; Zhang, J. W.; Mao, J. J.; Wang, D. S.; Li, Y. D. Synergistic modulation of the separation of photo-generated carriers via engineering of dual atomic sites for promoting photocatalytic performance. *Adv. Mater.* **2021**, *33*, 2105904.

[15] Duan, J. L.; Hu, T. Y.; Zhao, Y. Y.; He, B. L.; Tang, Q. W. Carbon-electrode-tailored all-inorganic perovskite solar cells to harvest solar and water-vapor energy. *Angew. Chem., Int. Ed.* **2018**, *57*, 5746–5749.

[16] Yang, L.; Nandakumar, D. K.; Miao, L. Q.; Suresh, L.; Zhang, D. W.; Xiong, T.; Vaghasiya, J. V.; Kwon, K. C.; Tan, S. C. Energy harvesting from atmospheric humidity by a hydrogel-integrated ferroelectric-semiconductor system. *Joule* **2020**, *4*, 176–188.

[17] Zhang, Y. X.; Nandakumar, D. K.; Tan, S. C. Digestion of ambient humidity for energy generation. *Joule* **2020**, *4*, 2532–2536.

[18] Zhang, Y. X.; Tan, S. C. Best practices for solar water production technologies. *Nat. Sustain.* **2022**, *5*, 554–556.

[19] Ding, H. Y.; Xin, Z. Q.; Yang, Y. Y.; Luo, Y. F.; Xia, K. L.; Wang, B. L.; Sun, Y. F.; Wang, J. P.; Zhang, Y. Y.; Wu, H. et al. Ultrasensitive, low-voltage operational, and asymmetric ionic sensing hydrogel for multipurpose applications. *Adv. Funct. Mater.* **2020**, *30*, 1909616.

[20] Wei, Q. M.; Ge, W. N.; Yuan, Z. C.; Wang, S. X.; Lu, C. G.; Feng, S. L.; Zhao, L.; Liu, Y. H. Moisture electricity generation: Mechanisms, structures, and applications. *Nano Res.* **2023**, *16*, 7496–7510.

[21] Wang, K. Q.; Xu, W. H.; Zhang, W.; Wang, X.; Yang, X.; Li, J. F.; Zhang, H. L.; Li, J. J.; Wang, Z. K. Bio-inspired water-driven electricity generators: From fundamental mechanisms to practical applications. *Nano Res. Energy* **2023**, *2*, e9120042.

[22] Zheng, S.; Tang, J. Y.; Lv, D.; Wang, M.; Yang, X.; Hou, C. S.; Yi, B.; Lu, G.; Hao, R. R.; Wang, M. Z. et al. Continuous energy harvesting from ubiquitous humidity gradients using liquid-infused nanofluidics. *Adv. Mater.* **2022**, *34*, 2106410.

[23] Zhou, S. Y.; Qiu, Z.; Strømme, M.; Xu, C. Solar-driven ionic power generation via a film of nanocellulose@conductive metal-organic framework. *Energy Environ. Sci.* **2021**, *14*, 900–905.

[24] Zhang, Y. X.; Yu, Z.; Qu, H.; Guo, S.; Yang, J. C.; Zhang, S. L.; Yang, L.; Cheng, S. A.; Wang, J.; Tan, S. C. Self-sustained programmable hygroelectronic interfaces for humidity-regulated hierarchical information encryption and display. *Adv. Mater.*, in press, https://doi.org/10.1002/adma.202208081.

[25] Zhang, Y. X.; Guo, S.; Yu, Z. G.; Qu, H.; Sun, W. X.; Yang, J. C.; Suresh, L.; Zhang, X. P.; Koh, J. J.; Tan, S. C. An asymmetric hygroscopic structure for moisture-driven hygro-ionic electricity generation and storage. *Adv. Mater.* **2022**, *34*, 2201228.

[26] Moreira, K. S.; Lermen, D.; dos Santos, L. P.; Galembeck, F.; Burgo, T. A. L. Flexible, low-cost and scalable, nanostructured conductive paper-based, efficient hygroelectric generator. *Energy Environ. Sci.* **2021**, *14*, 353–358.

[27] Wang, H. Y.; Sun, Y. L.; He, T. C.; Huang, Y. X.; Cheng, H. H.; Li, C.; Xie, D.; Yang, P. F.; Zhang, Y. F.; Qu, L. T. Bilayer of polyelectrolyte films for spontaneous power generation in air up to an integrated 1000 V output. *Nat. Nanotechnol.* **2021**, *16*, 811–819.

[28] Bai, J. X.; Hu, Y. J.; Guang, T. L.; Zhu, K. X.; Wang, H. Y.; Cheng, H. H.; Liu, F.; Qu, L. T. Vapor and heat dual-drive sustainable power for portable electronics in ambient environments. *Energy Environ. Sci.* **2022**, *15*, 3086–3096.

[29] Yang, C.; Huang, Y. X.; Cheng, H. H.; Jiang, L.; Qu, L. T. Hygroelectric generators: Rollable, stretchable, and reconfigurable graphene hygroelectric generators (Adv. Mater. 2/2019). *Adv. Mater.* **2019**, *31*, 1970013.

[30] Huang, Y. X.; Cheng, H. H.; Yang, C.; Yao, H. Z.; Li, C.; Qu, L. T. All-region-applicable, continuous power supply of graphene oxide composite. *Energy Environ. Sci.* **2019**, *12*, 1848–1856.

[31] Sun, Z. Y.; Wen, X.; Wang, L. M.; Ji, D. X.; Qin, X. H.; Yu, J. Y.; Ramakrishna, S. Emerging design principles, materials, and applications for moisture-enabled electric generation. *eScience* **2022**, *2*, 32–46.

[32] Wang, H. Y.; He, T. C.; Hao, X. Z.; Huang, Y. X.; Yao, H. Z.; Liu, F.; Cheng, H. H.; Qu, L. T. Moisture adsorption–desorption full cycle power generation. *Nat. Commun.* **2022**, *13*, 2524.

[33] Liu, X. M.; Gao, H. Y.; Ward, J. E.; Liu, X. R.; Yin, B.; Fu, T. D.; Chen, J. H.; Lovley, D. R.; Yao, J. Power generation from ambient humidity using protein nanowires. *Nature* **2020**, *578*, 550–554.

[34] Wang, D.; Jiang, J.; Cao, M. Y.; Xie, S. S.; Li, Y. M.; Chen, L. J.; Zhao, J. W.; Yang, G. Y. An unprecedented dumbbell-shaped pentadeca-nuclear W-Er heterometal cluster stabilizing nanoscale hexameric arsenotungstate aggregate and electrochemical sensing properties of its conductive hybrid film-modified electrode. *Nano Res.* **2021**, *15*, 3628–3637.

[35] Cameron, J. M.; Guillemot, G.; Galambos, T.; Amin, S. S.; Hampson, E.; Haidaraly, K. M.; Newton, G. N.; Izzet, G. Supramolecular assemblies of organo-functionalised hybrid polyoxometalates: From functional building blocks to hierarchical nanomaterials. *Chem. Soc. Rev.* **2022**, *51*, 293–328.

[36] Zhang, Y. F.; Li, Z. W.; Zhang, J. J.; Xu, L. L.; Han, Z. K.; Baiker, A.; Li, G. Nanostructured Ni-MoC$_x$: An efficient non-noble metal catalyst for the chemoselective hydrogenation of nitroaromatics. *Nano Res.*, in press, https://doi.org/10.1007/s12274-023-5598-x.

[37] Wang, J.; Wang, L.; Liu, C. Y.; Wang, Y.; Ye, F.; Yan, W.; Liu, B. Polyoxovanadate ionic crystals with open tunnels stabilized by macrocations for lithium-ion storage. *Nano Res.*, in press, https://doi.org/10.1007/s12274-023-5491-7.

[38] Jordan, J. W.; Cameron, J. M.; Lowe, G. A.; Rance, G. A.; Fung, K. L. Y.; Johnson, L. R.; Walsh, D. A.; Khlobystov, A. N.; Newton, G. N. Stabilization of polyoxometalate charge carriers via redox-driven nanoconfinement in single-walled carbon nanotubes. *Angew. Chem., Int. Ed.* **2022**, *61*, e202115619.

[39] Lin, L. H.; Wei, F. F.; Jiang, R.; Huang, Y. C.; Lin, S. The role of central heteroatom in electrochemical nitrogen reduction catalyzed by polyoxometalate-supported single-atom catalyst. *Nano Res.* **2023**, *16*, 309–317.

[40] Duan, S. J.; Xu, X. Y.; Chen, W. L.; Zhi, J. J.; Li, F. R. Grain boundaries passivation of high efficiency and stable perovskite photodetector by polyoxometalate-based composite SiW$_{11}$@ZIF-8. *Polyoxometalates* **2022**, *1*, 9140003.

[41] Li, J.; Zhang, D.; Chi, Y. N.; Hu, C. W. Catalytic application of polyoxovanadates in the selective oxidation of organic molecules. *Polyoxometalates* **2022**, *1*, 9140012.

[42] Wei, Y. G. Polyoxometalates: An interdisciplinary journal focused on all aspects of polyoxometalates. *Polyoxometalates* **2022**, *1*, 9140014.

[43] Zhang, S. M.; Shi, W. X.; Wang, X. Locking volatile organic molecules by subnanometer inorganic nanowire-based organogels. *Science* **2022**, *377*, 100–104.

[44] Liu, Q. D.; He, S. Q.; Yu, B.; Cheng, X. J.; Shi, W. X.; Wang, X. Visible light induced Ag-polyoxometalate coassembly into single-cluster nanowires. *Adv. Mater.* **2022**, *34*, 2206178.

[45] Zhao, D.; Zhuang, Z. W.; Cao, X.; Zhang, C.; Peng, Q.; Chen, C.; Li, Y. D. Atomic site electrocatalysts for water splitting, oxygen reduction, and selective oxidation. *Chem. Soc. Rev.* **2020**, *49*, 2215–2264.

[46] Xiong, Y.; Dong, J. C.; Huang, Z. Q.; Xin, P. Y.; Chen, W. X.; Wang, Y.; Li, Z.; Jin, Z.; Xing, W.; Zhuang, Z. B. et al. Single-atom Rh/N-doped carbon electrocatalyst for formic acid oxidation. *Nat. Nanotechnol.* **2020**, *15*, 390–397.

[47] Yang, D. R.; Zuo, S. W.; Yang, H. Z.; Wang, X. Single-unit-cell catalysis of CO$_2$ electroreduction over sub-1 nm Cu$_9$S$_5$ nanowires. *Adv. Energy Mater.* **2021**, *11*, 2100272.

[48] Liu, Q. D.; Zhang, Q. H.; Shi, W. X.; Hu, H. S.; Zhuang, J.; Wang, X. Self-assembly of polyoxometalate clusters into two-dimensional clusterphene structures featuring hexagonal pores. *Nat. Chem.* **2022**, *14*, 433–440.

[49] Zhang, H. Y.; Zhao, W. L.; Li, H. Q.; Zhuang, Q. H.; Sun, Z. Q.; Cui, D. Y.; Chen, X. J.; Guo, A.; Ji, X.; An, S. et al. Latest progress in covalently modified polyoxometalates-based molecular assemblies and advanced materials. *Polyoxometalates* **2022**, *1*, 9140011.

[50] Zhang, Y.; Liu, Y. F.; Wang, D.; Liu, J. C.; Zhao, J. W. State-of-the-art advances in the syntheses, structures, and applications of polyoxometalate-based metal-organic frameworks. *Polyoxometalates* **2023**, *2*, 9140017.

[51] Lu, M.; Zhang, M.; Liu, J.; Yu, T. Y.; Chang, J. N.; Shang, L. J.; Li, S. L.; Lan, Y. Q. Confining and highly dispersing single polyoxometalate clusters in covalent organic frameworks by covalent linkages for CO$_2$ photoreduction. *J. Am. Chem. Soc.* **2022**, *144*, 1861–1871.

[52] Liu, J. C.; Zhao, J. W.; Streb, C.; Song, Y. F. Recent advances on high-nuclear polyoxometalate clusters. *Coord. Chem. Rev.* **2022**, *471*, 214734.

[53] Luo, S.; Luo, Y. F.; Wu, H. C.; Li, M. Y.; Yan, L. J.; Jiang, K. L.; Liu, L.; Li, Q. Q.; Fan, S. S.; Wang, J. P. Self-assembly of 3D carbon nanotube sponges: A simple and controllable way to build macroscopic and ultralight porous architectures. *Adv. Mater.* **2017**, *29*, 1603549.

[54] Ji, S. F.; Chen, Y. J.; Wang, X. L.; Zhang, Z. D.; Wang, D. S.; Li, Y. D. Chemical synthesis of single atomic site catalysts. *Chem. Rev.* **2020**, *120*, 11900–11955.

[55] Miras, H. N.; Yan, J.; Long, D. L.; Cronin, L. Engineering polyoxometalates with emergent properties. *Chem. Soc. Rev.* **2012**, *41*, 7403–7430.

[56] Li, J. R.; Chen, M. J.; Zhou, S. J.; Li, H. G.; Hao, J. C. Self-assembly of fullerene C$_{60}$-based amphiphiles in solutions. *Chem. Soc. Rev.* **2022**, *51*, 3226–3242.

[57] Gumerova, N. I.; Rompel, A. Polyoxometalates in solution: Speciation under spotlight. *Chem. Soc. Rev.* **2020**, *49*, 7568–7601.

[58] Martin-Sabi, M.; Soriano-López, J.; Winter, R. S.; Chen, J. J.; Vilà-Nadal, L.; Long, D. L.; Galán-Mascarós, J. R.; Cronin, L. Redox tuning the Weakley-type polyoxometalate archetype for the oxygen evolution reaction. *Nat. Catal.* **2018**, *1*, 208–213.

[59] Gumerova, N. I.; Rompel, A. Synthesis, structures, and applications of electron-rich polyoxometalates. *Nat. Rev. Chem.* **2018**, *2*, 0112.

[60] Yang, L.; Lei, J.; Fan, J. M.; Yuan, R. M.; Zheng, M. S.; Chen, J. J.; Dong, Q. F. The intrinsic charge carrier behaviors and applications of polyoxometalate clusters based materials. *Adv. Mater.* **2021**, *33*, 2005019.

[61] Liu, R. J.; Streb, C. Polyoxometalate-single atom catalysts (POM-SACs) in energy research and catalysis. *Adv. Energy Mater.* **2021**, *11*, 2101120.

[62] Horn, M. R.; Singh, A.; Alomari, S.; Goberna-Ferrón, S.; Benages-Vilau, R.; Chodankar, N.; Motta, N.; Ostrikov, K.; MacLeod, J.; Sonar, P. et al. Polyoxometalates (POMs): From electroactive clusters to energy materials. *Energy Environ. Sci.* **2021**, *14*, 1652–1700.

[63] Fang, Z. H.; Luo, Y. F.; Liu, H. T.; Hong, Z. X.; Wu, H. C.; Zhao, F.; Liu, P.; Li, Q. Q.; Fan, S. S.; Duan, W. H. et al. Boosting the oxidative potential of polyethylene glycol-based polymer electrolyte to 4.36 V by spatially restricting hydroxyl groups for high-voltage flexible lithium-ion battery applications. *Adv. Sci.* **2021**, *8*, 2100736.

[64] Zhang, J.; Zhang, K. N.; Xia, B. Y.; Wei, Y.; Li, D. Q.; Zhang, K.; Zhang, Z. X.; Wu, Y.; Liu, P.; Duan, X. D. et al. Carbon-nanotube-confined vertical heterostructures with asymmetric contacts. *Adv. Mater.* **2017**, *29*, 1702942.

[65] Liu, Q. D.; He, P. L.; Yu, H. D.; Gu, L.; Ni, B.; Wang, D.; Wang, X. Single molecule-mediated assembly of polyoxometalate single-cluster rings and their three-dimensional superstructures. *Sci. Adv.* **2019**, *5*, eaax1081.

[66] Lyon, D. K.; Miller, W. K.; Novet, T.; Domaille, P. J.; Evitt, E.; Johnson, D. C.; Finke, R. G. Highly oxidation resistant inorganic-porphyrin analog polyoxometalate oxidation catalysts. 1. The synthesis and characterization of aqueous-soluble potassium salts of α_2-P$_2$W$_{17}$O$_{61}$(M^{n+}·OH$_2$)$^{(n-10)}$ and organic solvent soluble tetra-n-butylammonium salts of α_2-P$_2$W$_{17}$O$_{61}$(M^{n+}·OH$_2$)$^{(n-11)}$ (M = Mn^{3+}, Fe^{3+}, Co^{2+}, Ni^{2+}, Cu^{2+}). *J. Am. Chem. Soc.* **1991**, *113*, 7209–7221.

[67] Contant, R.; Richet, M.; Lu, Y. W.; Keita, B.; Nadjo, L. Isomerically pure α_1-monosubstituted tungstodiphosphates: Synthesis, characterization, and stability in aqueous solutions. *Eur. J. Inorg. Chem.* **2002**, *2002*, 2587–2593.

[68] Granadeiro, C. M.; Ferreira, R. A. S.; Soares-Santos, P. C. R.; Carlos, L. D.; Nogueira, H. I. S. Lanthanopolyoxometalates as building blocks for multiwavelength photoluminescent organic–inorganic hybrid materials. *Eur. J. Inorg. Chem.* **2009**, *2009*, 5088–5095.

[69] Geue, N.; Winpenny, R. E. P.; Barran, P. E. Structural

characterisation methods for supramolecular chemistry that go beyond crystallography. *Chem. Soc. Rev.* **2022**, *51*, 8–27.

[70] Qian, K.; Winans, R. E.; Li, T. Insights into the nanostructure, solvation, and dynamics of liquid electrolytes through small-angle X-ray scattering. *Adv. Energy Mater.* **2020**, *11*, 200282.

[71] Liu, Y. Y.; Gao, F. Y.; Ko, S.; Wang, C. Z.; Liu, H. H.; Tang, X. L.; Yi, H. H.; Zhou, Y. S. Superior catalytic performance within H_2O-vapor of W-modified $CoMn_2O_4/TiO_2$ catalyst for selective catalytic reduction of NO_x with NH_3. *Chem. Eng. J.* **2022**, *434*, 134770.

[72] Wang, D. Y.; Zhang, D. Z.; Yang, Y.; Mi, Q.; Zhang, J. H.; Yu, L. D. Multifunctional latex/polytetrafluoroethylene-based triboelectric nanogenerator for self-powered organ-like MXene/metal-organic framework-derived CuO nanohybrid ammonia sensor. *ACS Nano* **2021**, *15*, 2911–2919.

[73] Zhou, T.; Zhu, L. M.; Xie, L. L.; Han, Q.; Yang, X. L.; Cao, X. Y.; Ma, J. M. New insight on $K_2Zn_2V_{10}O_{28}$ as an advanced cathode for rechargeable aqueous zinc-ion batteries. *Small* **2022**, *18*, 2107102.

[74] Chen, Y. C.; Huang, Y.; Xu, M. J.; Asset, T.; Yan, X. X.; Artyushkova, K.; Kodali, M.; Murphy, E.; Ly, A.; Pan, X. Q. et al. Catalysts by pyrolysis: Direct observation of transformations during re-pyrolysis of transition metal-nitrogen-carbon materials leading to state-of-the-art platinum group metal-free electrocatalyst. *Mater. Today* **2022**, *53*, 58–70.

[75] McGregor, D.; Burton-Pye, B. P.; Howell, R. C.; Mbomekalle, I. M.; Lukens, W. W. Jr.; Bian, F.; Mausolf, E.; Poineau, F.; Czerwinski, K. R.; Francesconi, L. C. Synthesis, structure elucidation, and redox properties of ^{99}Tc complexes of lacunary Wells–Dawson polyoxometalates: Insights into molecular ^{99}Tc–metal oxide interactions. *Inorg. Chem.* **2011**, *50*, 1670–1681.

[76] Wang, T.; Xu, M.; Li, X. H.; Wang, C. L.; Chen, W. L. Highly dispersed redox-active polyoxometalates' periodic deposition on multi-walled carbon nanotubes for boosting electrocatalytic triiodide reduction in dye-sensitized solar cells. *Inorg. Chem. Front.* **2020**, *7*, 1676–1684.

[77] Zhang, S. M.; Shi, H. D.; Tang, J. W.; Shi, W. X.; Wu, Z. S.; Wang, X. Super-aligned films of sub-1 nm Bi_2O_3-polyoxometalate nanowires as interlayers in lithium-sulfur batteries. *Sci. China Mater.* **2021**, *64*, 2949–2957.

[78] Zhang, S. M.; Shi, W. X.; Siegler, T. D.; Gao, X. Q.; Ge, F.; Korgel, B. A.; He, Y.; Li, S. Z.; Wang, X. An all-inorganic colloidal nanocrystal flexible polarizer. *Angew. Chem., Int. Ed.* **2019**, *58*, 8730–8735.

[79] Liu, H. L.; Gong, Q. H.; Yue, Y. H.; Guo, L.; Wang, X. Sub-1 nm nanowire based superlattice showing high strength and low modulus. *J. Am. Chem. Soc.* **2017**, *139*, 8579–8585.

[80] Gunn, R. Thunderstorm electrification of hail and graupel by polar dribble. *Science* **1966**, *151*, 686–687.

[81] Gouveia, R. F.; Galembeck, F. Electrostatic charging of hydrophilic particles due to water adsorption. *J. Am. Chem. Soc.* **2009**, *131*, 11381–11386.

[82] Jin, D. W.; Ko, Y. J.; Ahn, C. W.; Hur, S.; Lee, T. K.; Jeong, D. G.; Lee, M.; Kang, C. Y.; Jung, J. H. Polarization- and electrode-optimized polyvinylidene fluoride films for harsh environmental piezoelectric nanogenerator applications. *Small* **2021**, *17*, 2007289.

[83] Chen, Z. M.; Gu, X. Q.; Guo, Y. T.; Wang, X.; Shao, M. W.; Dong, B.; Kang, Z. H. A carbon dot-based total green and self-recoverable solid-state electrochemical cell fully utilizing O_2/H_2O redox couple. *SusMat* **2021**, *1*, 448–457.

[84] Khan, M.; Hussain, A.; Malik, M. Y.; Salahuddin, T.; Aly, S. Numerical analysis of Carreau fluid flow for generalized Fourier's and Fick's laws. *Appl. Numer. Math.* **2019**, *144*, 100–117.

[85] Chen, F. R.; Chen, H. F. A diffusion model of the pervaporation separation of ethylene glycol-water mixtures through crosslinked poly(vinyl alcohol) membrane. *J. Membrane Sci.* **1998**, *139*, 201–209.

[86] Raut, D. R.; Mohapatra, P. K.; Choudhary, M. K.; Nayak, S. K. Evaluation of two calix-crown-6 ligands for the recovery of radio cesium from nuclear waste solutions: Solvent extraction and liquid membrane studies. *J. Membrane Sci.* **2013**, *429*, 197–205.